

**Damages induced by synchrotron radiation-based X-ray microanalysis
in chrome yellow paints and related Cr-compounds: assessment,
quantification and mitigation strategies**

Monico, L.; Cotte, M.; Vanmeert, F.; Amidani, L.; Janssens, K.; Nuyts, G.; Garrevoet, J.;
Falkenberg, G.; Glatzel, P.; Romani, A.; Miliari, C.;

Originally published:

September 2020

Analytical Chemistry 92(2020)20, 14164-14173

DOI: <https://doi.org/10.1021/acs.analchem.0c03251>

Perma-Link to Publication Repository of HZDR:

<https://www.hzdr.de/publications/Publ-31468>

Release of the secondary publication
on the basis of the German Copyright Law § 38 Section 4.

This document is confidential and is proprietary to the American Chemical Society and its authors. Do not copy or disclose without written permission. If you have received this item in error, notify the sender and delete all copies.

Damages induced by synchrotron radiation-based X-ray microanalysis in chrome yellow paints and related Cr-compounds: assessment, quantification and mitigation strategies

Journal:	<i>Analytical Chemistry</i>
Manuscript ID	ac-2020-03251s
Manuscript Type:	Article
Date Submitted by the Author:	31-Jul-2020
Complete List of Authors:	<p>Monico, Letizia; CNR, Istituto di Scienze e Tecnologie Chimiche "G. Natta" (SCITEC); University of Perugia, SMAArt Centre and Department of Chemistry, Biology and Biotechnology; University of Antwerp, AXES Research Group, NANOLab Centre of Excellence</p> <p>Cotte, Marine; ESRF; CNRS, LAMS</p> <p>Vanmeert, Frederik; University of Antwerp, AXES Research Group, NANOLab Centre of Excellence ; Laboratories of the Royal Institute of Cultural Heritage (KIK-IRPA)</p> <p>Amidani, Lucia; ESRF; Rossendorf Beamline at the ESRF, HZDR</p> <p>Janssens, Koen; University of Antwerp, AXES Research Group, NANOLab Centre of Excellence; Rijksmuseum, Conservation & Restoration-Scientific Research</p> <p>Nuyts, Gert; University of Antwerp, AXES Research Group, NANOLab Centre of Excellence</p> <p>Garrevoet, Jan ; DESY, Photon Science</p> <p>Falkenberg, Gerald; DESY, Photon Science</p> <p>Glatzel, P.; ESRF</p> <p>Romani, Aldo; Università degli Studi di Perugia, SMAArt Centre and Department of Chemistry, Biology and Biotechnology</p> <p>Miliani, Costanza; CNR, Istituto di Scienze del Patrimonio Culturale (ISPC)</p>

SCHOLARONE™
Manuscripts

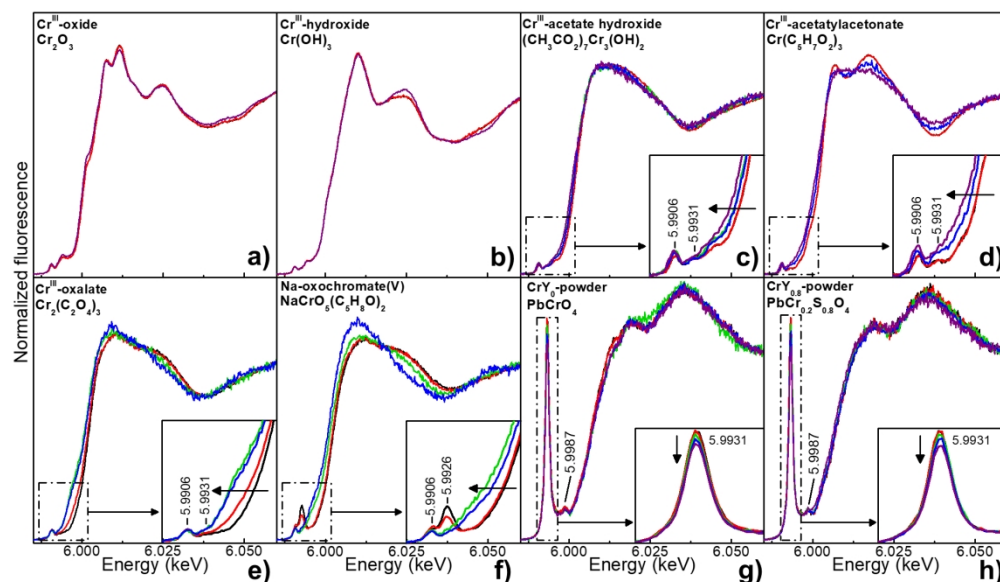


Figure 1. Cr K-edge XANES spectra of Cr-powders acquired at increasing fluences/doses at ESRF-ID21: (a) Cr^{III}-oxide, (b) Cr^{III}-hydroxide, (c) Cr^{III}-acetate hydroxide, (d) Cr^{III}-acetylacetonate, (e) Cr^{III}-oxalate, (f) Na-oxochromate(V), (g) CrY₀-powder, (h) CrY_{0.8}-powder [black: 1.7×10^7 ph/ μm^2 (0.1-0.6 MGy); red: 1.7×10^8 ph/ μm^2 (1-6 MGy); green: $\sim 5.7 \times 10^{11}$ ph/ μm^2 ($\sim 5 \times 10^3$ - 2×10^4 MGy); blue: $1-2 \times 10^{12}$ ph/ μm^2 ($\sim 9 \times 10^3$ - 4×10^4 MGy); purple: $1-2 \times 10^{13}$ ph/ μm^2 (~ 2 - 4×10^5 MGy)].

171x99mm (300 x 300 DPI)

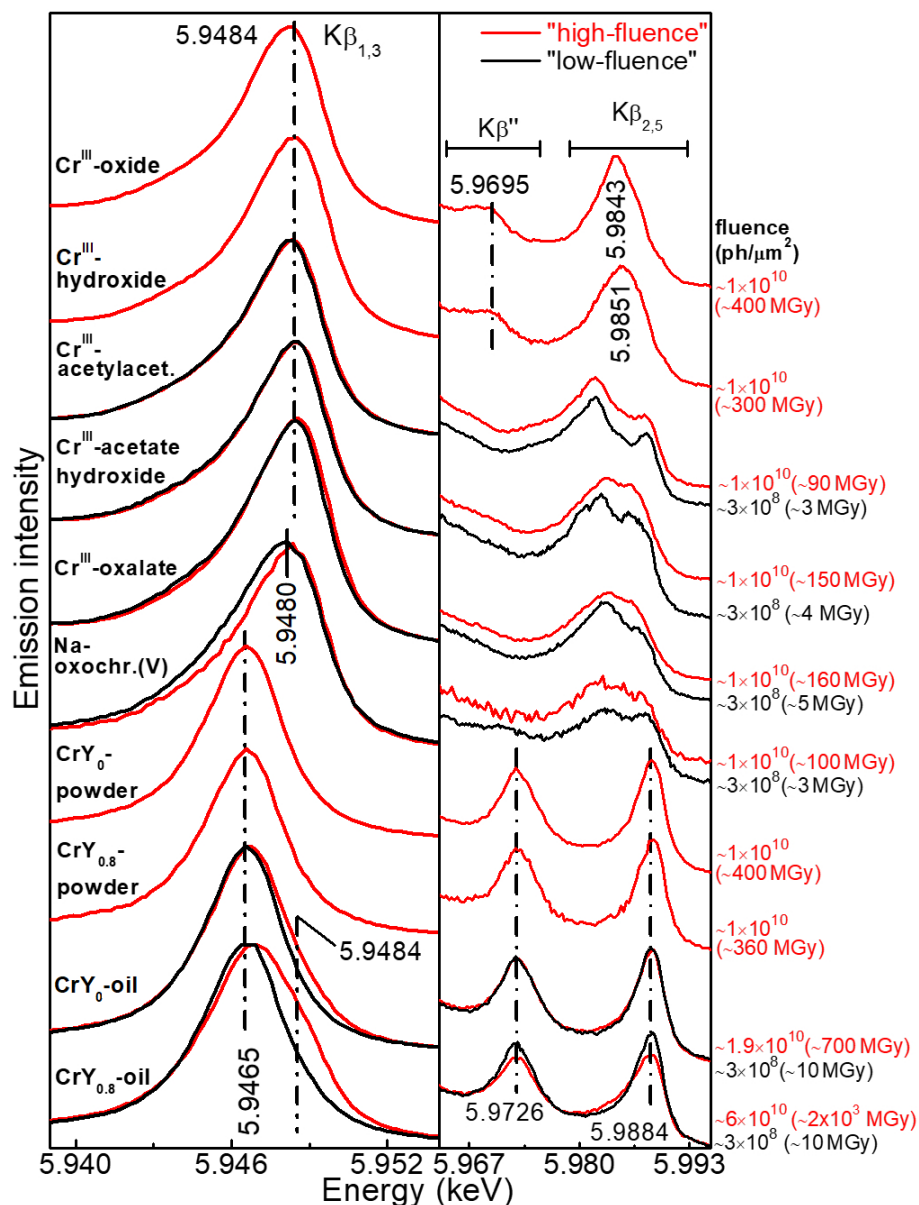


Figure 2. Cr-K β XES spectra of Cr-samples recorded using "high-fluence" (red) and "low-fluence" (black) conditions at ESRF-ID26: (left) K $\beta_{1,3}$ line; (right) K β satellite lines (see Figure S2 for the complete spectra of K β main lines). Fluences along with absorbed doses (in brackets) are also reported.

85x112mm (300 x 300 DPI)

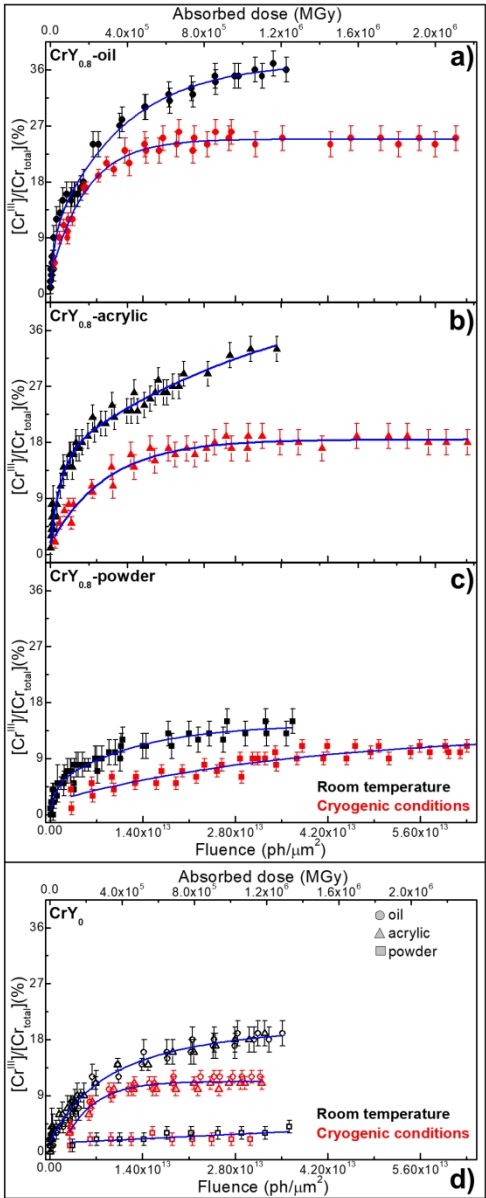


Figure 3. Plots of Cr^{III}-relative amount percentage vs. fluence/absorbed dose obtained at room temperature (black) and under cryogenic conditions (red) at ESRF-ID21: (a-c) CrY_{0.8}-samples; (d) CrY₀-samples. In blue, fit obtained using mono-exponential or bi-exponential functions.

85x210mm (300 x 300 DPI)

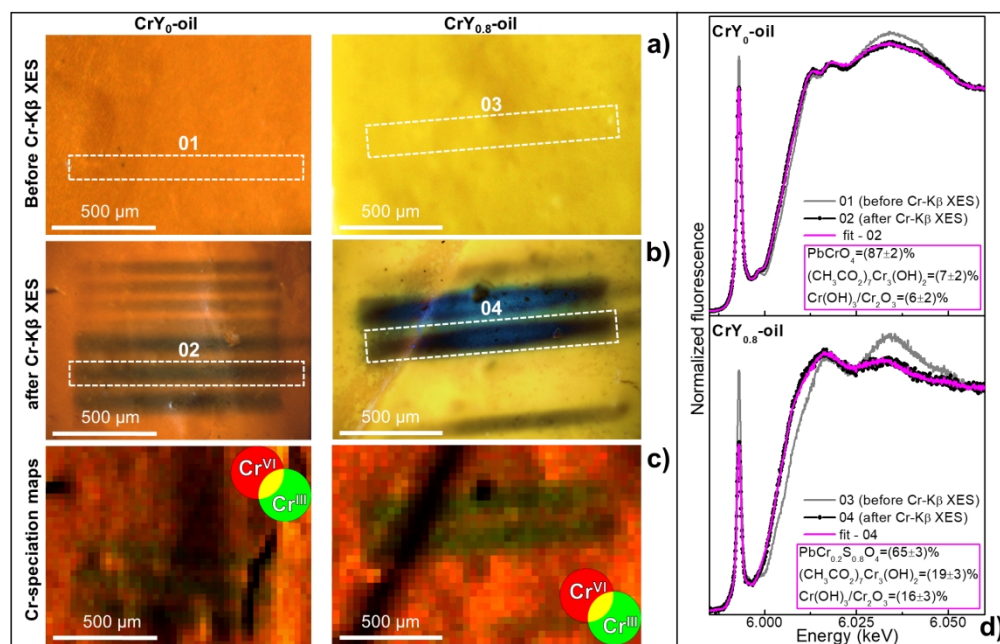


Figure 4. Photomicrographs of CrY₀-oil and CrY_{0.8}-oil (a) before and (b) after “high-fluence” Cr-Kβ XES investigations (*cf.* Figure 2 for the corresponding XES spectra). (c) RG composite SR μ-XRF Cr^{VI}/Cr^{III} maps recorded from the areas shown in (b) at ESRF-ID21 [step size (h×v): 30×30 μm²; exp. time: 100 ms/pixel]. (d) Cr K-edge XANES spectra (grey and black) recorded at ESRF-ID26 from the regions shown by the rectangles in (a,b) and corresponding LCF results (magenta).

180x115mm (300 x 300 DPI)

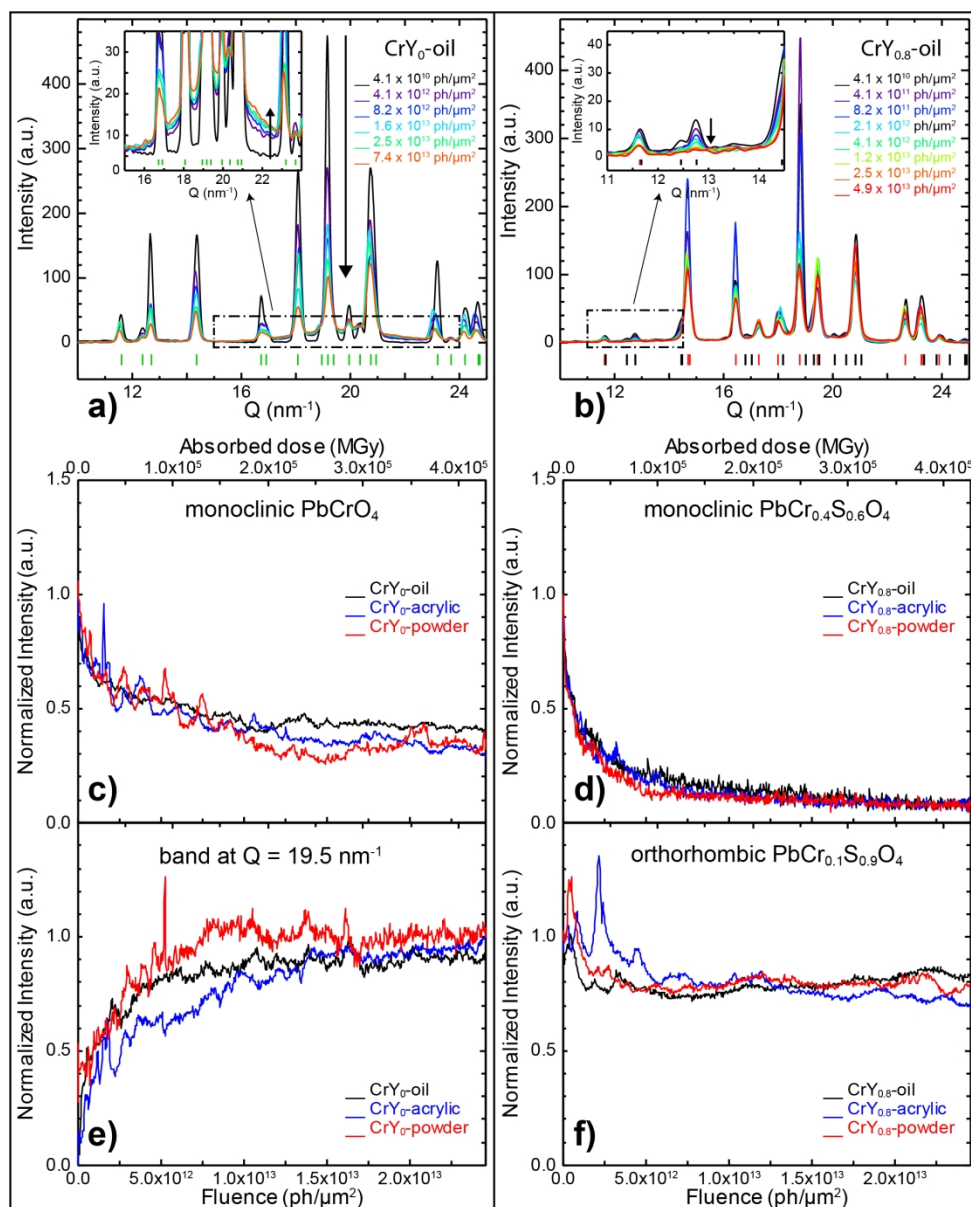


Figure 5. μ -XRD patterns collected from (a) CrY_0 -oil and (b) $\text{CrY}_{0.8}$ -oil at increasing fluences/doses at DESY-P06. Vertical bars indicate the diffraction peak positions of monoclinic PbCrO_4 (green), monoclinic $\text{PbCr}_{0.4}\text{S}_{0.6}\text{O}_4$ (black) and orthorhombic $\text{PbCr}_{0.1}\text{S}_{0.9}\text{O}_4$ (red). Normalized intensity or scaling factors vs. fluence/absorbed dose of (c) monoclinic PbCrO_4 , (d) monoclinic $\text{PbCr}_{0.4}\text{S}_{0.6}\text{O}_4$, (e) amorphous phase and (f) orthorhombic $\text{PbCr}_{0.1}\text{S}_{0.9}\text{O}_4$ in CrY_0 -/ $\text{CrY}_{0.8}$ -samples (black=oil; blue=acrylic; red=powder).

178x220mm (299 x 299 DPI)

Damages induced by synchrotron radiation-based X-ray microanalysis in chrome yellow paints and related Cr-compounds: assessment, quantification and mitigation strategies

Letizia Monico,^{1,2,3,*} Marine Cotte,^{4,5} Frederik Vanmeert,^{3,6} Lucia Amidani,^{4,7} Koen Janssens,^{3,8} Gert Nuyts,³ Jan Garrevoet,⁹ Gerald Falkenberg,⁹ Pieter Glatzel,⁴ Aldo Romani,^{1,2} Costanza Miliani¹⁰

¹ CNR-SCITEC, via Elce di Sotto 8, 06123 Perugia (Italy)

² SMAArt Centre and Department of Chemistry, Biology and Biotechnology, University of Perugia, via Elce di Sotto 8, 06123 Perugia (Italy)

³ AXES Research Group, NANOlaboratory Centre of Excellence, University of Antwerp, Groenenborgerlaan 171, 2020 Antwerp (Belgium)

⁴ ESRF, 71 avenue des martyrs, 38000 Grenoble (France)

⁵ LAMS, CNRS UMR 8220, Sorbonne Université, UPMC Univ Paris 06, 4 place Jussieu 75005, Paris (France)

⁶ Laboratories of the Royal Institute of Cultural Heritage (KIK-IRPA), Parc du Cinquanteenaire 1, 1000 Bruxelles (Belgium)

⁷ Rossendorf Beamline at the ESRF, HZDR, Institute of Resource Ecology, Dresden 01314, (Germany)

⁸ Rijksmuseum, Conservation & Restoration—Scientific Research, Hobbemastraat 22, 1071 ZC Amsterdam (The Netherlands)

⁹ DESY, Notkestraße 85, 22607 Hamburg (Germany)

¹⁰ CNR-ISPC, via Cardinale Guglielmo Sanfelice 8, 80134 Napoli (Italy)

*email: letizia.monico@cnr.it

Abstract

Synchrotron radiation (SR)-based X-ray methods are powerful analytical tools for several purposes and we widely use them for probing the degradation mechanisms of inorganic artists' pigments in paintings, including chrome yellows ($\text{PbCr}_{1-x}\text{S}_x\text{O}_4$; $0 \leq x \leq 0.8$), a class of compounds often found in Van Gogh masterpieces.

However, the high intensity and brightness of SR beams raise important issues regarding potential damages of the analyzed samples. A thorough knowledge of the SR X-ray sensitivity of each class of pigment in the painting matrix is therefore required to find analytical strategies that contribute to minimize the damage for preserving the integrity of the analyzed sample and to avoid misinterpretation of the data.

Here, we employ a combination of Cr K-edge X-ray absorption near edge structure (XANES) spectroscopy, Cr-K β X-ray emission spectroscopy (XES) and X-ray diffraction (XRD) to monitor and quantify the effects of SR X-rays on the stability of chrome yellows and related Cr-compounds and to define strategies for mitigating their damage.

We found that the SR X-ray beam exposure induces changes in the oxidation state and local coordination environment of Cr-ions and leads to a loss of the compound's crystalline structure. The extent of X-ray damage depends on some intrinsic properties of the samples (chemical composition of the pigment as well as the presence/absence and nature of the binder) and it can be minimized by optimizing the overall fluence/dose released to the samples and by working in vacuum and cryogenic conditions.

1. Introduction

The use of synchrotron radiation (SR)-based X-ray methods to study cultural heritage objects has seen a considerable increase over the last two decades due to their capabilities to provide spatially resolved elemental, molecular and structural speciation information down to the submicrometer scale.^{1,2} In such context, X-ray diffraction (XRD), X-ray fluorescence (XRF) and X-ray absorption near edge structure (XANES) spectroscopy are considered non-destructive techniques and they have been widely exploited to unveil the composition and degradation mechanisms of a number of constituents of different kinds of artefacts.^{1,2,3,4}

However, SR beams are orders of magnitude more intense and brighter than conventional laboratory sources, thus raising important issues regarding potential damage of the analyzed objects/samples.⁵

Irreversible changes have been observed for some inorganic pigments, including Prussian blue ($MFe^{III}[Fe^{II}(CN)_6] \cdot xH_2O$; $M=K^+, NH_4^+, Na^+$)^{6,7,8} and ultramarine blue [approximated as $(NaCa)_8[Al_6Si_6O_{24}](SO_4, S, Cl)_2$].^{9,10} In the case of Prussian blue, it was found that SR used for Fe K-edge XANES investigations may cause the fading of the pigment, by inducing a conversion from Fe^{III} to Fe^{II} . The extent of the damage depends on several factors, such as the sample conditioning during measurements and the substrate nature.⁶⁻⁸ For a series of natural and synthetic ultramarine blue pigments, changes in the S-K edge XANES spectra revealed that SR X-ray irradiation promotes a redox process which leads to the transformation of polysulfides (more likely $[S_6]^{-2}$ and $[S_8]^{-2}$) into S_3^{\bullet} radicals.⁹ For micro-samples taken from discolored ultramarine areas of early 20th century oil paintings, comparison of light microscopy images before and after Al K-edge XANES investigations showed a darkening of the surface which, whilst not affecting the features of the XANES spectra, should be considered if samples are to be used for further analysis.¹⁰

SR-based X-ray methods have been successfully employed for elucidating the degradation mechanisms of other inorganic pigments in oil paintings, such as vermilion (HgS),¹¹ red lead (Pb_3O_4),¹² cadmium yellows ($\text{Cd}_{1-x}\text{Zn}_x\text{S}$; $0 \leq x \leq 0.3$),^{13,14,15,16,17,18} orpiment/realgar (arsenic sulfides),^{19,20,21,22} zinc yellows ($\text{K}_2\text{O} \cdot 4\text{ZnCrO}_4 \cdot 3\text{H}_2\text{O}$),²³ chrome yellows ($\text{PbCr}_{1-x}\text{S}_x\text{O}_4$; $0 \leq x \leq 0.8$).^{24,25,26,27,28,29,30} However, a thorough knowledge of their sensitivity towards X-ray exposure is still lacking.

Understanding the nature and magnitude of damages induced by SR X-ray exposure and defining strategies of analysis to mitigate such damages is of great importance to preserve the integrity of the analyzed sample and to avoid misinterpretation of the data.

Here, we discuss the impact of monochromatic SR X-ray macro-/micro-beams on the stability of chrome yellow pigments and paints and we define a safe analytical protocol for their analysis.

Chrome yellows are known for their tendency to undergo darkening when exposed to UVA-visible light.^{24,31} By using SR-based Cr K-edge XANES in combination with electron paramagnetic resonance spectroscopy, we established that the darkening of chrome yellows in a number of Van Gogh paintings and artificially aged mock-ups is due to the photoreduction of the original Cr^{VI} to Cr^{III} -compounds, with Cr^{V} -species arising from the interaction between the pigment and the binder.^{24-28,31,32,33} We also found that Cr-reduction is favored by the presence of the binder and it is stronger in $\text{PbCr}_{1-x}\text{S}_x\text{O}_4$ solid solutions ($0 < x \leq 0.8$) with respect to monoclinic PbCrO_4 .^{29,33}

In this work, we focus on the SR X-ray stability of a set of $\text{Cr}^{\text{III}}/\text{Cr}^{\text{V}}$ -compounds and two chrome yellow types: (a) the monoclinic PbCrO_4 and (b) the mainly orthorhombic $\text{PbCr}_{0.2}\text{S}_{0.8}\text{O}_4$ (i.e. pigments with properties similar to those identified in paintings).³⁴

The chrome yellows were investigated in the absence and presence of two binders: linseed oil and a water-based acrylic emulsion. Although the former is the mainly used with chrome yellows by 19th-20th century painters,^{26,35} the two binders were chosen due to their different

1
2
3 contribution on the Cr^{VI}-reduction, being more significant when the pigment is mixed with
4
5 linseed oil rather than with acrylic.³³
6

7 By combining SR-based Cr K-edge XANES spectroscopy, Cr-K β X-ray emission
8 spectroscopy (XES) and μ -XRD we obtained semi-quantitative information about Cr-
9
10 speciation changes induced by SR X-ray exposure and we correlated them to intrinsic
11
12 properties of the samples and to a number of experimental parameters (e.g.
13
14 fluence/absorbed dose, ambient pressure, temperature). After discussing the results
15
16 obtained and describing how they may introduce data misinterpretation in the study of
17
18 chrome yellows degradation, we present experimental strategies to mitigate the SR X-ray-
19
20 induced damage for this class of pigments.
21
22
23
24
25
26
27
28
29
30
31
32
33
34
35
36
37
38
39
40
41
42
43
44
45
46
47
48
49
50
51
52
53
54
55
56
57
58
59
60

2. Experimental section

2.1. Materials

2.1.1 Reference compounds. The following Cr-powders were analyzed: lead chromate (PbCrO_4) and sulfur-rich lead chromate ($\text{PbCr}_{0.2}\text{S}_{0.8}\text{O}_4$), which are yellow pigments synthesized in our laboratory (for further information see ref ³⁴). Cr^{III} -oxide (Cr_2O_3), Cr^{III} -acetylacetonate [$\text{Cr}(\text{C}_5\text{H}_7\text{O}_2)_3$], Cr^{III} -acetate hydroxide [$(\text{CH}_3\text{CO}_2)_7\text{Cr}_3(\text{OH})_2$], sodium bis(2-hydroxy-2 methylbutyrato)-oxochromate(V) [$\text{NaCrO}_5(\text{C}_5\text{H}_8\text{O})_2$; hereafter denoted “Na-oxochromate(V)”] (Sigma-Aldrich), Cr^{III} -hydroxide [$\text{Cr}(\text{OH})_3$], Cr^{III} -oxalate [$\text{Cr}_2(\text{C}_2\text{O}_4)_3$] (City Chemical LLC), which are instead compounds selected based on previous studies,^{24-29,31-33} being the most likely degradation products of chrome yellow paints.

For experiments at beamlines ESRF-ID21 and DESY-P06, finely milled powders were prepared as a thin layer fixed onto adhesive tape; for measurements at beamline ESRF-ID26, the powders were investigated as pellets (13 mm diameter) diluted with boron nitride.

2.1.2 Paint mock-ups. Samples were prepared on polycarbonate slices using powders of either monoclinic PbCrO_4 or mainly orthorhombic $\text{PbCr}_{0.2}\text{S}_{0.8}\text{O}_4$ in mixture with either one of the following binders in a 4:1 weight ratio: linseed oil (Zecchi) or Primal B60-A (C.T.S.) (henceforward denoted “acrylic”).

All paints were left to dry in the dark at 25-35°C temperature and 35-45% relative humidity (i.e., indoor temperature and humidity measured by a thermohygrometer) for ~1 month and then directly analyzed without any additional preparation.

2.2 Analytical methods

2.2.1 μ -XRF and μ -XANES at Cr K-edge. Measurements were performed at the scanning X-ray micro-spectroscopy end-station of beamline ID21 of the European Synchrotron Radiation Facility (ESRF, Grenoble).³⁶ A Si(220) double-crystal monochromator was used to scan the X-ray beam energy across the Cr K-edge (5.97–6.10 keV). For the calibration, the first inflection point of the first-order derivative Cr K-edge XANES spectrum of a Cr metallic foil was set-up at 5.9892 keV. A photon flux between 2×10^8 ph/s and 1×10^{10} ph/s (varied using Al attenuators of 20–100 μm thickness) was employed during the experiment. At the exit of the monochromator, the beam size was defined using pinholes (50–100 μm diameter) for macro-XANES characterization. In these conditions, the fluence rate was $\sim 10^5$ – 10^6 ph/s $\cdot\mu\text{m}^2$. For μ -XANES investigations, the incident beam was focused with a Kirkpatrick-Baez (KB) mirror system down to a spot size of $\sim 1.0 \times 0.3 \mu\text{m}^2$ (h \times v). In these conditions, without beam attenuation, the fluence rate is typically $\sim 10^{10}$ ph/s $\cdot\mu\text{m}^2$. For normalization purposes, a photodiode upstream the sample is constantly monitoring the beam intensity.

XRF mapping was performed *via* raster-scanning the samples with 100 ms/pixel dwell times and using a 80 mm² collimated active area silicon drift diode detector (Xflash 5100, Bruker). The PyMca software³⁷ was used to obtain the elemental and Cr-oxidation state maps (see SI for details).

For each sample an unexposed spot was selected and a series of XRF-mode XANES spectra was acquired there to follow the spectral evolution as a function of the fluence (ph/ μm^2) and absorbed dose (MGy). The acquisition time was 75 s per spectrum. Measurements were performed under vacuum (10^{-4} – 10^{-5} mbar) both at room and cryogenic temperatures (sample stage cooled down to $\sim -150^\circ\text{C}$ by conductive Cu braids connected to a LN₂ filled Dewar).³⁸

The ATHENA software³⁹ was used for normalization and for linear combination fitting (LCF) of the spectra using a library of Cr-references spectra (see SI for details).

2.2.2 Cr-K β XES and Cr K-edge high-energy resolution fluorescence detected (HERFD)-XANES. Investigations were performed at beamline ID26 of the ESRF. The incident energy was selected using a Si(311) double-crystal monochromator. The emission spectrometer based on Rowland geometry was equipped with four spherically bent Ge(333) crystal analyzers (R=1000 mm). A Cr metallic foil was used to calibrate the incident energy, performed by setting the first inflection point of the first-order derivative to 5.989 keV. Samples were investigated in a fluorescence geometry oriented at 45° with respect to both the incident beam and the central analyzer crystal. The beam footprint size on the sample, determined by a pair of slits close to the sample, was 0.15 mm vertically and either 0.707 mm (slits at 0.5 mm) or 0.99 mm (slits at 0.7 mm) horizontally. The total flux varied from 1×10^{10} to 4×10^{12} ph/s, depending on the slit size and the presence of attenuators of different thickness (Figure S1).

XES measurements were performed with a 6.1 keV incident energy using two modalities: i) recording the full spectrum at a single point (henceforth denoted “high-fluence”); ii) collecting each energy point of the spectrum at a different sample spot (hereafter called “low-fluence”). The spectra acquired with mode ii) were also corrected for Cr concentration inhomogeneities. The second mode was implemented to minimize spectral changes due to X-ray exposure; thus, the integration time per point was adapted to the Cr-concentration and the sensitivity of the sample towards X-rays.

The K β main line spectra were recorded in the 5.91-5.96 keV range, with 0.2 eV energy increments and 2-7 s/point exposure time (total acquisition time for “high-fluence” spectra: ~250-1740 s). The profiles of K β satellite lines were measured in the 5.951-6.021 keV range, with energy step sizes of 1-0.3 eV and 1-14 s/point exposure time (total acquisition time for “high-fluence” spectra: ~390-2180 s).

To set the integration time per point needed to record XES spectra (“low-fluence mode”) with the minimum damage, a series of Cr K-edge HERFD-XANES spectra were acquired at an unexposed spot of the sample. The irradiation time before observing damage on HERFD-XANES was then taken as the total scanning time for XES. HERFD-XANES were also acquired before and after XES in “high-fluence mode” to evaluate the damage induced by the XES scan.

XES data were processed using PyMca.³⁷ The normalization and LCF of the XANES spectra was performed *via* ATHENA.³⁹

2.2.3 μ -XRD. Investigations were carried out at beamline P06 of PETRA-III (DESY, Hamburg).⁴⁰ KB-mirrors were used to focus the primary beam of 21 keV to a spot of $0.65 \times 0.75 \mu\text{m}^2$ ($v \times h$) and a flux of $\sim 2 \times 10^{10}$ ph/s. Diffraction patterns were collected by a PILATUS 300K area detector (Dectris Ltd., CH), positioned at *ca.* 140 mm behind the sample to capture d-spacing values between 1.4–20 nm (Q-values between 3–45 nm^{-1}). Calibration was performed by analyzing a LaB_6 reference.

A series of diffraction patterns were collected each second, while exposing the same spot to the X-ray beam for a period of 600 s or 1800 s. Azimuthal integration of the 2D diffraction images and data fitting was performed using the XRDUA software.⁴¹ All non-overlapping diffraction signals with d-spacing values between 1.4–10 nm as well as a broad band ($Q = 19.5 \text{ nm}^{-1}$) were fitted with Gaussian profiles. The background was modelled using a stripping function. The sum of the peak areas of a given compound was used to describe its crystalline intensity.

3. Results and Discussion

3.1 Cr-powders: nature of the SR X-ray-induced damage

To evaluate the effects of SR X-rays on different Cr-compounds, we started to analyze a set of Cr-powders (i.e. not mixed with the binder) by recording at a selected point of each sample a series of Cr K-edge XANES spectra at increasing fluences.

XANES was selected as primary monitoring method for its high sensitivity to the oxidation states and the local coordination environments of Cr-ions.^{24,42,43,44,45} The pre-edge structures are attributed to transitions into orbitals with Cr 3d character. In octahedral Cr^{III}-compounds (Figure 1a-e), orbitals with metal p and d character cannot mix due inversion symmetry and the spectral intensity arises from quadrupole transition matrix elements resulting in weak pre-edge peaks at 5.9906 and 5.9931 keV. For tetrahedral Cr^V- and Cr^{VI}-compounds (Figure 1f-h), the pre-edge gains intensity from dipole-allowed transitions because orbitals with p and d symmetry can mix, appearing as a single peak (t_2 symmetry) of variable intensity at 5.9926 and 5.9931 keV, respectively. Differences in the features of the post-edge absorption region reflect the different Cr local environments in the respective crystal structures.⁴²⁻⁴⁵

Regarding the effects of SR X-rays on Cr^{III}-compounds, fluences in the 1.7×10^7 - 1.0×10^{13} ph/ μm^2 range (~ 0.4 - 3×10^5 MGy) did not induce any detectable change in the XANES spectra of Cr₂O₃ and Cr(OH)₃ (Figure 1a,b). Meaningful modifications occurred instead in the profiles of organo-Cr^{III} complexes starting from $\sim 1.7 \times 10^8$ ph/ μm^2 (~ 1 -2 MGy) (Figure 1c-e: red line). For such compounds, the shift of the absorption edge position towards lower energies is clearly visible along with changes in the relative intensity of the two weak pre-edge peaks. For Cr^{III}-acetylacetonate and Cr^{III}-oxalate a loss of structure and broadening of the post-edge features is visible too (Figure 1d,e). Such changes point out that the SR X-ray exposure induces modifications to the Cr^{III}-ions local coordination environment.^{42,43,45}

As expected,⁴⁶ Na-oxochromate(V) shows a significant sensitivity under the SR X-ray beam exposure (Figure 1f). For fluences greater than 1.7×10^7 ph/ μm^2 (~ 0.1 MGy), the reduction of Cr^{V} to Cr^{III} -compounds is revealed by the shift of the absorption edge towards lower energies and the progressive decrease of the intensity ratio between the bands at 5.9926 and 5.9906 keV. Under comparable fluences, similar but less pronounced changes are observable in the XANES profiles of PbCrO_4 and $\text{PbCr}_{0.2}\text{S}_{0.8}\text{O}_4$ powders (hereafter denoted CrY_0 and $\text{CrY}_{0.8}$, respectively) (Figure 1g,h). With increasing fluences up to 1.0×10^{13} ph/ μm^2 ($\sim 4 \times 10^5$ MGy), the pre-edge peak intensity (quantitatively proportional to the Cr^{VI} to total Cr content ratio)^{25,31} decreases for both $\text{CrY}_{0.8}$ (15%) and CrY_0 (10%) (purple line).

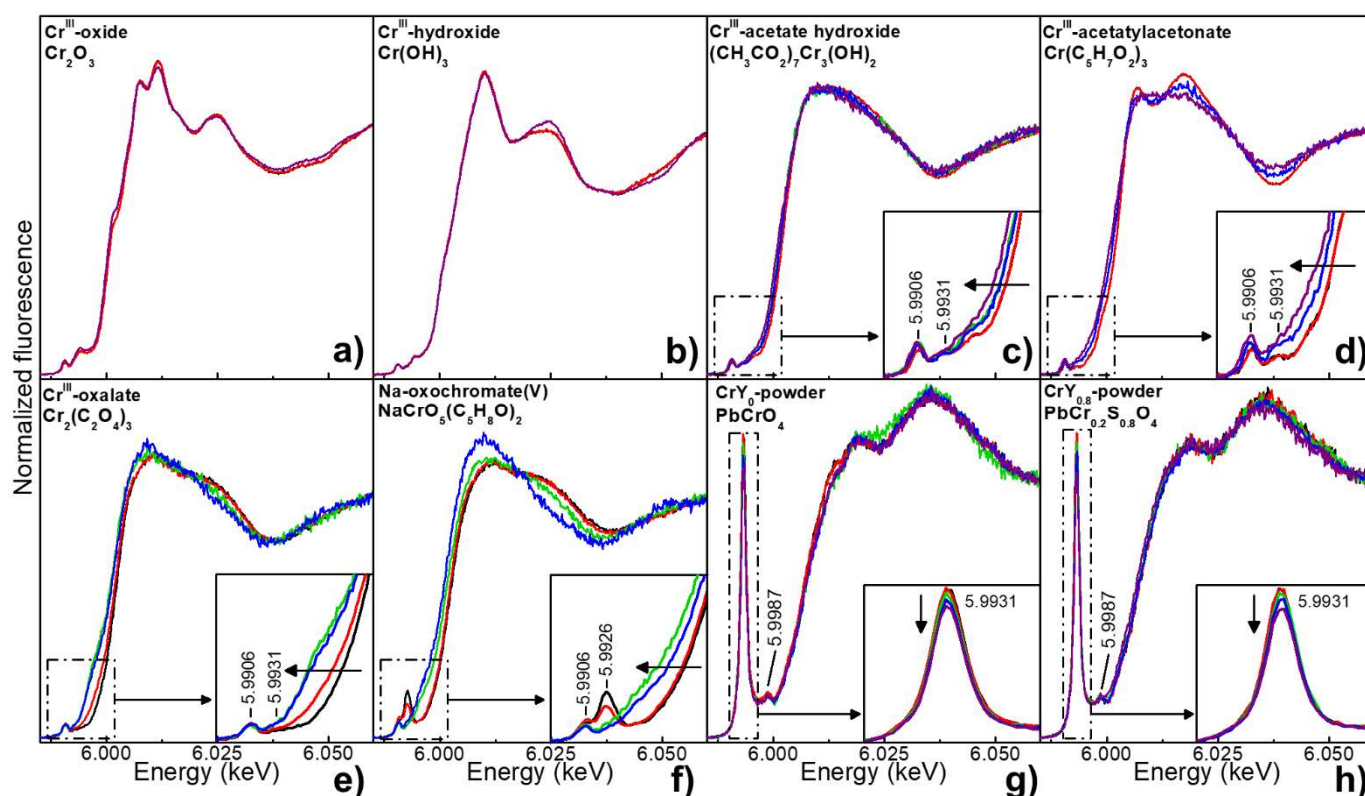


Figure 1. Cr K-edge XANES spectra of Cr-powders acquired at increasing fluences/doses at ESRF-ID21: (a) Cr^{III} -oxide, (b) Cr^{III} -hydroxide, (c) Cr^{III} -acetate hydroxide, (d) Cr^{III} -acetylacetonate, (e) Cr^{III} -oxalate, (f) Na-oxochromate(V), (g) CrY_0 -powder, (h) $\text{CrY}_{0.8}$ -powder [black: 1.7×10^7 ph/ μm^2 (0.1-0.6 MGy); red: 1.7×10^8 ph/ μm^2 (1-6 MGy); green: $\sim 5.7 \times 10^{11}$ ph/ μm^2 ($\sim 5 \times 10^3$ - 2×10^4 MGy); blue: 1 - 2×10^{12} ph/ μm^2 ($\sim 9 \times 10^3$ - 4×10^4 MGy); purple: 1 - 2×10^{13} ph/ μm^2 (~ 2 - 4×10^5 MGy)].

With the aim to get complementary information to XANES, we then analyzed the Cr-powders by Cr-K β XES. So far, this method has never been used to study the degradation of chrome yellows. Cr-K β valence-to-core (vtc) XES can discriminate ligands with similar atomic number in the first coordination sphere of Cr-ions,^{47,48,49,50} thus it is expected to help understanding the nature of Cr^{III}-/Cr^V-degradation products in chrome yellow paints.

The K β emission spectra of Cr-powders consist of two different regions.⁴⁷⁻⁵¹ The first one includes the K $\beta_{1,3}$ main line and a weak band at lower energy named K β' and it results from a core-to-core 3p \rightarrow 1s transition (Figure 2: leftmost panel; Figure S2). Such lines are sensitive to the unpaired electrons in the Cr 3d orbitals, thus providing information on the Cr-oxidation state: as the oxidation state increases, the K $\beta_{1,3}$ position shifts to lower energies, while the K β' intensity decreases. The second region shows the K β satellite lines (Figure 2: rightmost panel). These features arise from vtc transitions, involving electrons occupying valence molecular orbitals having ligand p or s type character which fills-in Cr 1s orbital, and includes the K $\beta_{2,5}$ line and K β'' or cross-over peak. The K β'' intensity and position are sensitive to the ligand (L) nature and show strong dependency on the chromium's local symmetry,⁵¹ being more intense and shifted at higher energies in tetrahedral CrY₀ and CrY_{0.8} samples than in octahedral Cr^{III}-oxides. The K β'' intensity also depends on the magnitude of Cr-L orbital overlap,⁴⁸ thus providing a reasonable explanation to why such band is very weak in the organo-Cr^{III} and Cr^V complexes profiles. In the spectra of Cr-oxides, organo-Cr^{III}/Cr^V complexes and Cr^{VI}-compounds, changes of the K $\beta_{2,5}$ shape and position reflect instead the different nature of the Cr-L chemical bond.

Cr-K β XES spectra of organo-Cr^{III} and -Cr^V complexes recorded at "high-fluence" ($\sim 10^{10}$ ph/ μm^2 ; Figure 2: red lines) show important differences with respect to the "low-fluence" ones ($\sim 10^8$ ph/ μm^2 ; black lines). For organo-Cr^{III} compounds, while no changes are visible in the K β main lines, a loss of structure and broadening is visible in the K β satellite lines. In line with Cr K-edge μ -XANES results (Figure 1), such changes are attributable to

modifications of the Cr^{III} -ions local coordination environment. For the Cr^{V} -compound, the “high-fluence” conditions have promoted the reduction of Cr^{V} to Cr^{III} -species along with changes in the Cr-ions coordination. This is proved by the shift towards higher energies of $\text{K}\beta_{1,3}$ band and by modifications of the shape of $\text{K}\beta$ satellite lines. No meaningful changes are observed between the “high-fluence” and the “low-fluence” spectra of Cr_2O_3 , $\text{Cr}(\text{OH})_3$, CrY_0 -powder and $\text{CrY}_{0.8}$ -powder (only the formers are shown in Figure 2).

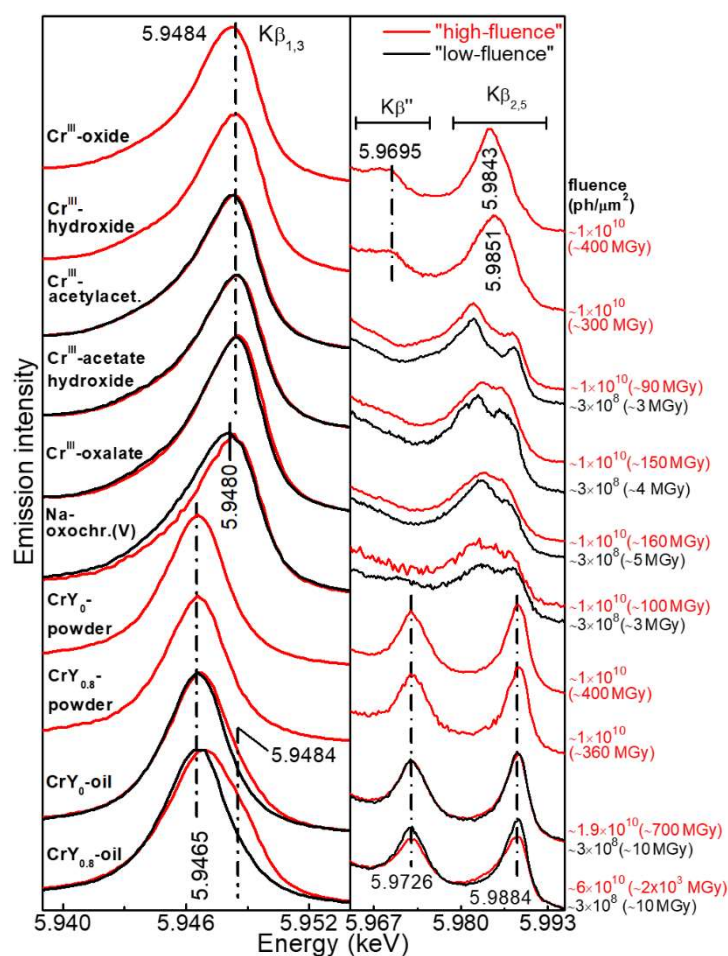


Figure 2. Cr- $\text{K}\beta$ XES spectra of Cr-samples recorded using “high-fluence” (red) and “low-fluence” (black) conditions at ESRF-ID26: (left) $\text{K}\beta_{1,3}$ line; (right) $\text{K}\beta$ satellite lines (see Figure S2 for the complete spectra of $\text{K}\beta$ main lines). Fluences along with absorbed doses (in brackets) are also reported.

3.2 Chrome yellow paints: effects of the binder and quantification of the SR X-ray-induced damage

To monitor and quantitatively evaluate the effects of SR X-rays on chrome yellows in relation to the presence and nature of the binder, we then performed a series of damage tests on paint mock-ups prepared by mixing CrY₀ or CrY_{0.8}-powders with either linseed oil or acrylic.

Figure 3 (black symbols) shows the plots of Cr^{III}-relative amount percentage vs. fluence/absorbed dose obtained via LCF of different Cr-references to the series of XANES spectra recorded from each chrome yellow sample at room temperature (see Figure S3 for details). The Cr^{III}-abundance exponentially increases with increasing fluence up to $\sim 3.5 \times 10^{13}$ ph/ μm^2 ($\sim 1.2 \times 10^6$ MGy), achieving its highest value for CrY_{0.8}-oil ($\sim 35\%$). Under the same irradiation conditions, the reactivity of CrY_{0.8}-acrylic is higher than that of CrY_{0.8}-powder, being the final Cr^{III}-amount of $\sim 30\%$ and $\sim 10\%$, respectively. The tendency of CrY₀-samples to undergo reduction is lower than that of the equivalent CrY_{0.8} ones. Notably, CrY₀-oil and CrY₀-acrylic reveal a similar stability under SR X-ray exposure, giving rise to the formation of Cr^{III}-abundances not greater than 20%. For CrY₀-powder, the Cr^{III}-amount remains below 5%. For both chrome yellow types, the increased tendency to undergo photo-reduction in the presence of the binder can be justified considering the strong sensitivity of organic materials under SR X-ray irradiation. Organic bonds can be easily broken, thus giving rise to radicals, which can further contribute to Cr^{VI}-reduction.^{5,33}

Under “high-fluence” conditions, changes in XES data are also more pronounced for CrY_{0.8} and when the oil is present (Figure 2, CrY₀-oil and CrY_{0.8}-oil spectra). The K $\beta_{1,3}$ broadening, through the presence of shoulder at ~ 5.9484 keV, and variations in the relative intensity of K β satellite lines are attributable to the formation of Cr^{III}-compounds and modifications of Cr-ions coordination.

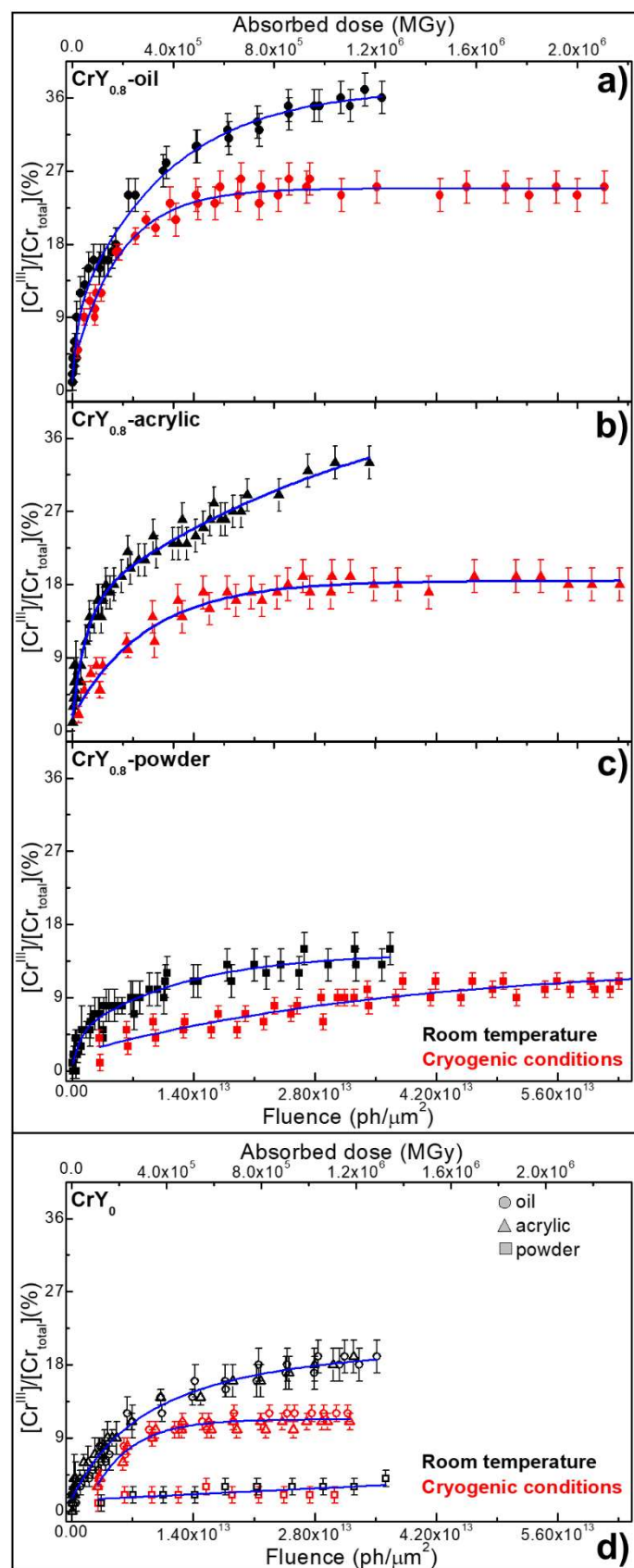


Figure 3. Plots of Cr^{III} -relative amount percentage vs. fluence/absorbed dose obtained at room temperature (black) and under cryogenic conditions (red) at ESRF-ID21: **(a-c)** $\text{CrY}_{0.8}$ -samples; **(d)** CrY_0 -samples. In blue, fit obtained using mono-exponential or bi-exponential functions.

Chemical changes induced by “high-fluence” XES occur along with a permanent darkening of the paint surface (Figure 4a,b). Such phenomenon is not apparent in the same samples analyzed at “low-fluence”. Cr K-edge μ -XANES analysis of darkened areas permitted to monitor and quantitatively evaluate the extent of damage (Figure 4c,d). As expected, before XES, the μ -XANES spectra resemble to the ones typically obtained for chrome yellows;²⁴ after XES, Cr-oxidation state maps combined with μ -XANES measurements show that the darkened areas contain higher Cr^{III}-amounts in CrY_{0.8}-oil (~35%) than in CrY₀-oil (~13%). Vibrational micro-spectroscopies revealed that the alteration of the binder has also occurred in addition to that of the pigment (Figure S4).

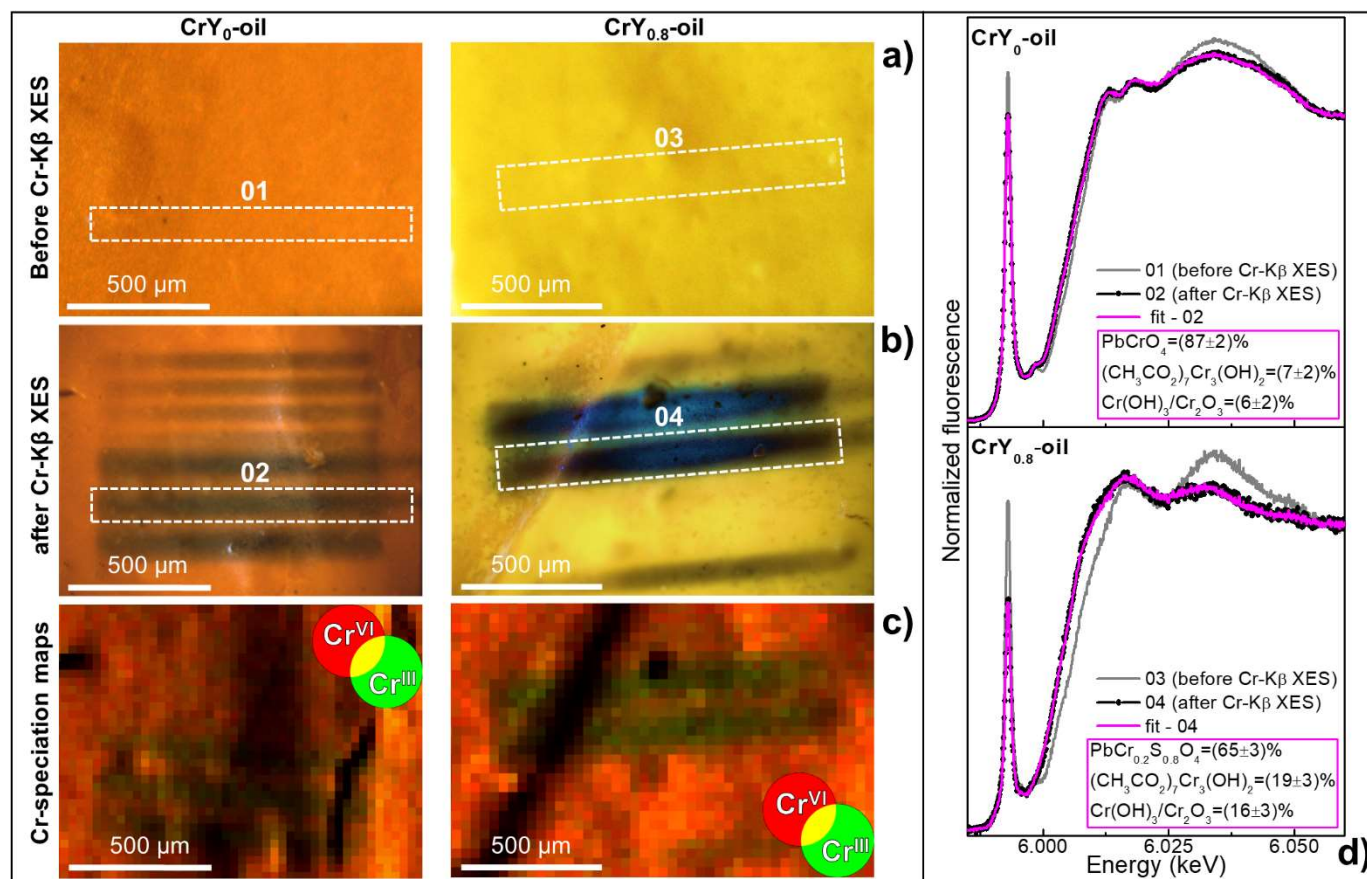


Figure 4. Photomicrographs of CrY₀-oil and CrY_{0.8}-oil (a) before and (b) after “high-fluence” Cr-K β XES investigations (cf. Figure 2 for the corresponding XES spectra). (c) RG composite SR μ -XRF Cr^{VI}/Cr^{III} maps recorded from the areas shown in (b) at ESRF-ID21 [step size (h \times v): 30 \times 30 μ m²; exp. time: 100 ms/pixel]. (d) Cr K-edge XANES spectra (grey and black) recorded at ESRF-ID26 from the regions shown by the rectangles in (a,b) and corresponding LCF results (magenta).

In Figure 5a,b, XRD patterns obtained at increasing fluences/doses are shown for CrY₀-/CrY_{0.8}-oil paints. As earlier reported,³⁴ CrY₀ contains only monoclinic PbCrO₄ (Figure 5a: green bars), while monoclinic PbCr_{0.4}S_{0.6}O₄ and orthorhombic PbCr_{0.1}S_{0.9}O₄ are present in CrY_{0.8} (Figure 5b: black and red bars). For both monoclinic structures, the intensity of their diffraction peaks decreases with increasing fluence/dose (Figure 5c,d), indicating a loss in crystallinity. For a fluence of 7.5×10^{12} ph/ μm^2 ($\sim 1.5 \times 10^5$ MGy), the PbCr_{0.4}S_{0.6}O₄ diffraction intensity decreases to ~ 10 - 20% in all CrY_{0.8}-samples, while that of PbCrO₄ is diminished to 40 - 50% in the CrY₀-samples for the same fluence. The conversion of crystalline monoclinic phases into a poorly structured/amorphous material with increasing fluences/doses is suggested by the formation of a broad band (at $Q=19.5 \text{ nm}^{-1}$). For CrY₀-samples (Figure 5a, inset), it occurs starting from ~ 2 - 4×10^{11} ph/ μm^2 (~ 4 - 8×10^3 MGy) and its intensity gradually increases up to $\sim 1.5 \times 10^{13}$ ph/ μm^2 ($\sim 2.5 \times 10^5$ MGy). For CrY_{0.8}-samples, such signal can hardly be seen due to the low abundance of PbCr_{0.4}S_{0.6}O₄.³⁴

While the monoclinic phases show a strong X-ray sensitivity, the diffraction intensity of orthorhombic PbCr_{0.1}S_{0.9}O₄ (the most abundant compound in CrY_{0.8}) stays fairly unchanged over the entire fluence range. Its intensity drops to $\sim 80\%$ at 7.5×10^{12} ph/ μm^2 ($\sim 1.5 \times 10^5$ MGy) and does not change further up to 2.5×10^{13} ph/ μm^2 ($\sim 4 \times 10^5$ MGy) (Figure 5f).

The darkened areas caused by μ -XRD in CrY-oil paints were further investigated by Cr-speciation analysis, revealing that the X-ray exposure has also led to the formation of Cr^{III}-compounds (Figure S5).

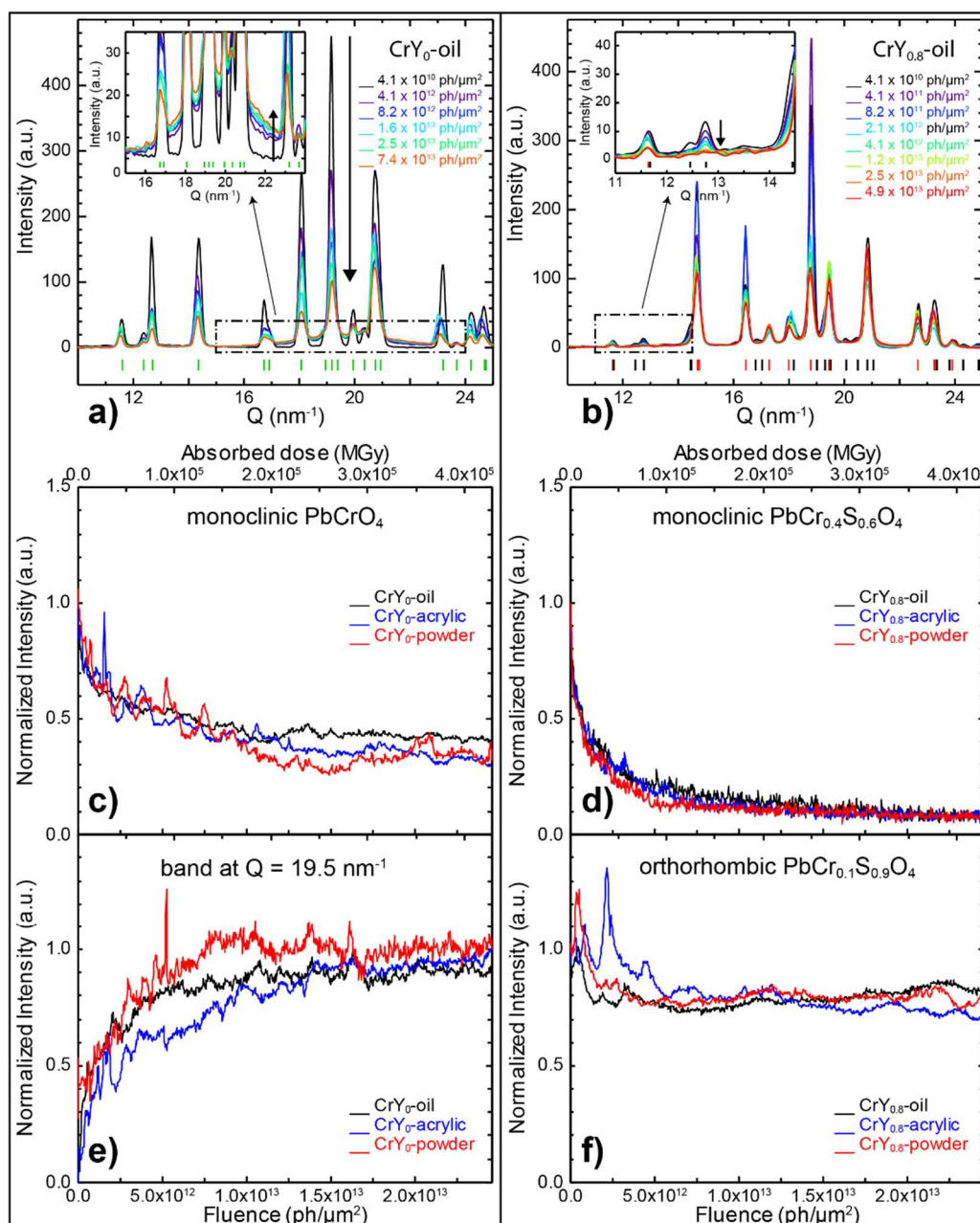


Figure 5. μ -XRD patterns collected from (a) CrY_0 -oil and (b) $\text{CrY}_{0.8}$ -oil at increasing fluences/doses at DESY-P06. Vertical bars indicate the diffraction peak positions of monoclinic PbCrO_4 (green), monoclinic $\text{PbCr}_{0.4}\text{S}_{0.6}\text{O}_4$ (black) and orthorhombic $\text{PbCr}_{0.1}\text{S}_{0.9}\text{O}_4$ (red). Normalized intensity or scaling factors vs. fluence/absorbed dose of (c) monoclinic PbCrO_4 , (d) monoclinic $\text{PbCr}_{0.4}\text{S}_{0.6}\text{O}_4$, (e) amorphous phase and (f) orthorhombic $\text{PbCr}_{0.1}\text{S}_{0.9}\text{O}_4$ in CrY_0 -/ $\text{CrY}_{0.8}$ -samples (black=oil; blue=acrylic; red=powder).

3.3. Mitigation strategies for SR X-ray-induced damage in chrome yellows

3.3.1 Optimization of the fluence/dose. When measuring *via* SR X-ray sources, the first thing to do to acquire data with minimum sample damage is to assess the threshold fluence/dose where spectral changes induced by X-ray exposure shows up in the data. At ESRF-ID21 and ESRF-ID26 (Figures 1-3; X-ray energy: ~6 keV) such values are about 5×10^{11} ph/ μm^2 ($\sim 2 \times 10^4$ MGy) and 10^8 ph/ μm^2 (~ 10 MGy), respectively, and the difference is mainly due to the use of vacuum at ESRF-ID21. At DESY-P06 (Figure 5; X-ray energy: 21 keV) this is $\sim 1\text{--}2 \times 10^{11}$ ph/ μm^2 ($\sim 2\text{--}4 \times 10^3$ MGy).

Once the threshold fluence/dose under specific conditions has been determined, the data acquisition time should be adapted to stay below the threshold value when possible (Figures 1-3,5). If fast-data acquisition is not feasible, an alternative is to decrease the flux of the incoming beam (e.g. using attenuators of different thickness; see Figure S6) as long as adequate signal-to-noise-ratio are maintained. When the fluence/dose limit is reached and statistic is not good enough, one can analyse several spots on the sample. However, this is feasible only when spatial resolution is not an issue and if samples are sufficiently large (order of tenths mm^2) and compositionally homogenous (Figure 2, “low-fluence” data). Defocusing the beam is another strategy to minimize the fluence/dose to the sample, but sometimes at the expense of spectral resolution (e.g. XES analysis).

3.3.2. Measuring under vacuum conditions. For similar doses, the photo-induced reduction is less pronounced for samples analyzed at ESRF-ID21, with respect to those investigated at ESRF-ID26 and DESY-P06. For example, in the case of $\text{CY}_{0.8}$ -oil, measurements performed at room temperature using $\sim 2 \times 10^3$ MGy at ESRF-ID21 and ESRF-ID26 led to the production of Cr^{III} -abundances smaller than 5% and of $\sim 35\%$, respectively (Figures 3a,4d). In the same sample, experiments carried out using $\sim 8 \times 10^5$ MGy at ESRF-ID21 and DESY-P06 induced the formation of Cr^{III} -amounts of $\sim 35\%$ and $\sim 45\%$, respectively (Figure 3a, Figure S5). The lower Cr^{III} -abundances obtained at ESRF-

ID21 can be explained considering that these measurements were conducted under vacuum conditions. According to literature,⁵ such sample environment may contribute to indirectly slowing down Cr-reduction due to the absence/neglectable content of air gases (e.g. O₂) and moisture, which favor the oxidative degradation of the binder.

3.3.3. Lowering the temperature. Cryo-preservation is routinely used for the study of biological systems.^{52,53} Cooling results in a reduction of diffusive processes and hinders the extensive propagation of ions and radicals.^{5,54} Such strategy is rarely considered for the analysis of artistic materials. Thus, we decided to assess its efficiency for chrome yellows. Figure 3 shows the comparison between the plots of Cr^{III}-amount percentage vs. fluence/absorbed dose recorded from chrome yellow samples at room temperature (black symbols) and under cryogenic conditions (red symbols). At low temperature, the (smaller) reactivity of CrY₀-powder remains the same under SR X-ray irradiation (Figure 3d), while the photo-induced Cr^{VI}-reduction slows down for all the other samples. Compared to the room temperature measurements, the final Cr^{III}-amount is decreased of ~40-45% for CrY_{0.8}-acrylic, CrY₀-oil and CrY₀-acrylic (Figure 3b,d), and it is diminished of ~30% for CrY_{0.8}-oil and CrY_{0.8}-powder (Figure 3a,c). Thus, similarly to what was already observed for other Cr-based materials in different contexts,^{46,55} measuring spectra at cryogenic temperature contributes to mitigate the SR X-ray-induced damage of chrome yellows.

4. Conclusions

In this work, a combination of SR-based X-ray techniques, namely Cr K-edge XANES, Cr-K β XES and μ -XRD, allowed us to monitor and quantify the X-ray-induced damage in chrome yellows and related Cr-compounds and to define strategies to mitigate such damage.

Our results proved that SR X-rays induce changes in the oxidation state and local coordination environment of Cr-ions and promote changes of the compound's crystalline structure.

Under equivalent irradiation conditions, the extent of damage depends on the nature of the analysed sample. Organo-Cr^{III}-complexes are more prone to change than Cr^{III}-oxides. For chrome yellows (PbCrO₄ and PbCr_{0.2}So_{0.8}O₄), modifications are more pronounced for the PbCr_{0.2}So_{0.8}O₄ type and when the pigment is mixed with the binder. This result shows how crucial it is to evaluate X-ray sensitivity on systems as similar as possible to the real paints, rather than on pure powders. Studies about SR X-ray-induced effects on the binder in chrome yellow paints are still ongoing, and their results will be published in follow-up papers.

One first strategy to minimize the X-ray-induced damage of chrome yellows is to employ fluences not greater than 10¹⁰-10¹¹ ph/ μ m². The use of larger solid angle detectors,^{27,56} may contribute to further reduce the overall dose released to samples. Two other strategies consist in working in vacuum and cryogenic conditions. Cryo-preservation is expected to be more regularly employed for future analysis of X-ray sensitive mock-ups and historical painting fragments. However, a long-term monitoring of samples will be required to assess the occurrence of any delayed damages due to temperature changes. Related to that, where feasible, the preparation of paint thin-sections by a microtome should be considered, so as to keep the rest of the cross-section available for other experiments.

If the X-ray-induced damage cannot be fully prevented, it is important to: i) quantitatively assess its contribution to the signal; ii) analyse all samples with the same exposure

1
2
3 conditions; iii) well-document the damage to prevent erroneous future analyses. Generally,
4
5 care should be taken when comparing data obtained using different X-ray beams and
6
7 sample conditioning during analysis at various beamlines.
8
9

10 Overall, our findings contribute to define a safe analytical protocol for chrome yellows
11
12 investigations by SR X-ray methods, which allows for avoiding misinterpretations of data
13
14 finalized to the study of their degradation mechanism and to prevent damage of historical
15
16 samples.
17
18
19
20
21
22
23
24
25
26
27
28
29
30
31
32
33
34
35
36
37
38
39
40
41
42
43
44
45
46
47
48
49
50
51
52
53
54
55
56
57
58
59
60

Associated Content

Supporting Information

The Supporting Information is available free of charge at xxxx

Cr-oxidation state mapping and LCF of Cr K-edge XANES spectra; determination of photon flux at ESRF-ID26; additional XES/XANES and vibrational micro-spectroscopy data on chrome yellow samples; Relationship between the X-ray photo-induced Cr^{VI}-reduction and fluence rate.

Acknowledgments

The research was financially supported by: the EU projects IPERION-CH (grant agreement no. 654028, H2020-INFRAIA-2014-2015) and CALIPSOplus (grant agreement no. 730872, H2020-EU.1.4.1.2.); the project AMIS (Dipartimenti di Eccellenza 2018-2022, funded by MIUR and Perugia University). For the beamtime grants received, we thank: ESRF-ID21/ID26 (experiment nos. HG64, HG129, HG98; in-house beamtimes). Portions of this research was performed at Petra-III, P06 at DESY, a member of the Helmholtz Association (HGF) (experiment nos. I-20160672 EC, I-20170721 EC). L.M. acknowledges the Erasmus+ Programme (Staff Mobility for training, 2018-2019).

References

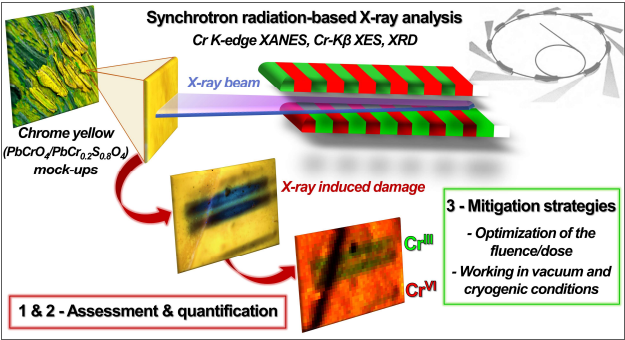
- ¹ Bertrand, L.; Bernard, S.; Marone, F.; Thoury, M.; Reiche, I.; Gourrier, A.; Sciau, P.; Bergmann U. *Top. Curr. Chem.* **2016**, *374*, 1-39.
- ² Cotte, M.; Genty-Vincent, A.; Janssens, K.; Susini, J. *C. R. Phys.* **2018**, *19*, 575-588.
- ³ Janssens, K.; Van der Snickt, G.; Vanmeert, F.; Legrand, S.; Nuyts, G.; Alfeld, M.; Monico, L.; Anaf, W.; De Nolf, W.; Vermeulen, M.; Verbeeck, J.; De Wael, K. *Top. Curr. Chem.* **2016**, *374*, 77-128.
- ⁴ Gonzalez, V.; Cotte, M.; Vanmeert, F.; De Nolf, W.; Janssens, K. *Chem.-Eur. J.* **2020**, *26*, 1703-1719.
- ⁵ Bertrand, L.; Schöeder, S.; Anglos, D.; Breese, M.B.; Janssens, K.; Moini, M.; Simon, A. *TrAC, Trends Anal. Chem.* **2015**, *66*, 128-145.
- ⁶ Gervais, C.; Languille, M.A.; Reguer, S.; Gillet, M.; Vicenzi, E.P.; Chagnot, S.; Baudalet, F.; Bertrand, L. *Appl. Phys. A: Mater. Sci. Process.* **2013**, *111*, 15-22.
- ⁷ Gervais, C.; Languille, M.A.; Moretti, G.; Réguer, S. *Langmuir* **2015**, *31*, 8168-8175.
- ⁸ Gervais, C.; Thoury, M.; Réguer, S.; Gueriau, P.; Mass, J. *Appl. Phys. A: Mater. Sci. Process.* **2015**, *121*, 949-955.
- ⁹ Ganio, M.; Pouyet, E. S.; Webb, S. M.; Patterson, C.M.S.; Walton, M.S. *Pure Appl. Chem.* **2018**, *90*, 463-475.
- ¹⁰ Cato, E.; Borca, C.; Huthwelker, T.; Ferreira, E.S. *Microchem. J.* **2016**, *126*, 18-24.
- ¹¹ Radepon, M.; De Nolf, W.; Janssens, K.; Van der Snickt, G.; Coquinot, Y.; Klaassen, L.; Cotte, M. *J. Anal. At. Spectrom.* **2011**, *26*, 959-968.
- ¹² Vanmeert, F.; Van der Snickt, G.; Janssens, K. *Angew. Chem., Int. Ed.* **2015**, *54*, 3607-3610.
- ¹³ Mass, J.L.; Opila, R.; Buckley, B.; Cotte, M.; Church, J.; Mehta, A. *Appl. Phys. A: Mater. Sci. Process.* **2013**, *111*, 59-68.
- ¹⁴ Pouyet, E.; Cotte, M.; Fayard, B.; Salomé, M.; Meirer, F.; Mehta, A.; Uffelman, E.S.; Hull, A.; Vanmeert, F.; Kieffer, J.; Burghammer, M.; Janssens, K.; Sette, F.; Mass, J. *Appl. Phys. A: Mater. Sci. Process.* **2015**, *121*, 967-980.
- ¹⁵ Van der Snickt, G.; Dik, J.; Cotte, M.; Janssens, K.; Jaroszewicz, J.; De Nolf, W.; Groenewegen, J.; Van der Loeff, L. *Anal. Chem.* **2009**, *81*, 2600-2610.

- ¹⁶ Van der Snickt, G.; Janssens, K.; Dik, J.; De Nolf, W.; Vanmeert, F.; Jaroszewicz, J.; Cotte, M.; Falkenberg, G.; Van der Loeff, L. *Anal. Chem.* **2012**, *84*, 10221-10228.
- ¹⁷ Monico, L.; Chieli, A.; De Meyer, S.; Cotte, M.; De Nolf, W.; Falkenberg, G.; Janssens, K.; Romani, A.; Miliani, C. *Chem.-Eur. J.* **2018**, *24*, 11584-11593.
- ¹⁸ Monico, L.; Cartechini, L.; Rosi, F.; Chieli, A.; Grazia, C.; De Meyer, S.; Nuyts, G.; Vanmeert, F.; Janssens, K.; Cotte, M.; De Nolf, W.; Falkenberg, G.; Crina Anca Sandu, I.; Storevik Tveit, E.; Mass, J.; Pereira de Freitas, R.; Romani, A.; Miliani, C. *Sci. Adv.* **2020**, *6*, eaay3514, doi: 10.1126/sciadv.aay3514.
- ¹⁹ Keune, K.; Mass, J.; Meirer, F.; Pottasch, C.; van Loon, A.; Hull, A.; Church, J.; Pouyet, E.; Cotte, M.; Mehta, A. *J. Anal. At. Spectrom.* **2015**, *30*, 813-827.
- ²⁰ Vermeulen, M.; Nuyts, G.; Sanyova, J.; Vila, A.; Buti, D.; Suuronen, J. P.; Janssens, K. *J. Anal. At. Spectrom.* **2016**, *31*, 1913-1921.
- ²¹ Keune, K.; Mass, J.; Mehta, A.; Church, J.; Meirer, F. *Heritage Sci.* **2016**, *4*, 10, doi: 10.1186/s40494-016-0078-1.
- ²² Simoen, J.; De Meyer, S.; Vanmeert, F.; de Keyser, N.; Avranovich, E.; Van der Snickt, G.; Van Loon, A.; Keune, K.; Janssens, K. *Heritage Sci.* **2019**, *7*, 83, doi: 10.1186/s40494-019-0324-4.
- ²³ Zanella, L.; Casadio, F.; Gray, K.A.; Warta, R.; Mac, Q.; Gaillard, J.F. *J. Anal. At. Spectrom.* **2011**, *26*, 1090-1097.
- ²⁴ Monico, L.; Van der Snickt, G.; Janssens, K.; De Nolf, W.; Miliani, C.; Verbeeck, J.; Tian, H.; Tan, H.; Dik, J.; Radepont, M.; Cotte, M. *Anal. Chem.* **2011**, *83*, 1214-1223.
- ²⁵ Monico, L.; Van der Snickt, G.; Janssens, K.; De Nolf, W.; Miliani, C.; Dik, J.; Radepont, M.; Hendriks, E.; Geldof, M.; Cotte, M. *Anal. Chem.* **2011**, *83*, 1224-1231.
- ²⁶ Monico, L.; Janssens, K.; Vanmeert, F.; Cotte, M.; Brunetti, B.G.; Van der Snickt, G.; Leeuwestein, M.; Salvant Plisson, J.; Menu, M.; Miliani, C. *Anal. Chem.* **2014**, *86*, 10804-10811.
- ²⁷ Monico, L.; Janssens, K.; Alfeld, M.; Cotte, M.; Vanmeert, F.; Ryan, C.G.; Falkenberg, G.; Howard, D.L.; Brunetti, B.G.; Miliani, C. *J. Anal. At. Spectrom.* **2015**, *30*, 613-626.
- ²⁸ Monico, L.; Janssens, K.; Hendriks, E.; Vanmeert, F.; Van der Snickt, G.; Cotte, M.; Falkenberg, G.; Brunetti, B.G.; Miliani, C. *Angew. Chem., Int. Ed.* **2015**, *54*, 13923-13927.

- ²⁹ Monico, L.; Janssens, K.; Miliani, C.; Van der Snickt, G.; Brunetti, B.G.; Cestelli Guidi, M.; Radepont, M.; Cotte, M. *Anal. Chem.* **2013**, *85*, 860-867.
- ³⁰ Otero, V.; Vilarigues, M.; Carlyle, L.; Cotte, M.; De Nolf, W.; Melo, M.J. *Photochem. Photobiol. Sci.* **2018**, *17*, 266-270.
- ³¹ Monico, L.; Janssens, K.; Cotte, M.; Romani, A.; Sorace, L.; Grazia, C.; Brunetti, B.G.; Miliani, C. *J. Anal. At. Spectrom.* **2015**, *30*, 1500-1510.
- ³² Monico, L.; Janssens, K.; Cotte, M.; Sorace, L.; Vanmeert, F.; Brunetti, B.G.; Miliani, C. *Microchem. J.* **2016**, *124*, 272-282.
- ³³ Monico, L.; Sorace, L.; Cotte, M.; De Nolf, W.; Janssens, K.; Romani, A.; Miliani, C. *ACS Omega* **2019**, *4*, 6607-6619.
- ³⁴ Monico, L.; Janssens, K.; Miliani, C.; Brunetti, B.G.; Vagnini, M.; Vanmeert, F.; Falkenberg, G.; Abakumov, A.; Lu, Y.; Tian, H.; Verbeeck, J.; Radepont, M.; Cotte, M.; Hendriks, E.; Geldof, M.; van der Loeff, L.; Salvant, J.; Menu, M. *Anal. Chem.* **2013**, *85*, 851-859.
- ³⁵ Roy, A. *National Gallery Technical Bulletin* **2007**, *28*, 58-68.
- ³⁶ Cotte, M.; Pouyet, E.; Salome, M.; Rivard, C.; De Nolf, W.; Castillo-Michel, H.; Fabris, T.; Monico, L.; Janssens, K.; Wang, T.; Sciau, P.; Verger, L.; Cormier, L.; Dargaud, O.; Brun, E.; Bugnazet, D.; Fayard, B.; Hesse, B.; Pradas del Real, A.; Veronesi, G.; Langlois, J.; Balcar, N.; Vandenberghe, Y.; Sole, V.A.; Kieffer, J.; Barrett, R.; Cohen, C.; Cornu, C.; Baker, R.; Gagliardini, E.; Papillon, E.; Susini, J. *J. Anal. At. Spectrom.* **2017**, *32*, 477-493.
- ³⁷ Cotte, M.; Fabris, T.; Agostini, G.; Motta Meira, D.; De Viguerie, L.; Solé, V.A. *Anal. Chem.* **2016**, *88*, 6154-6160.
- ³⁸ Salomé, M.; Cotte, M.; Baker, R.; Barrett, R.; Benseny-Cases, N.; Berruyer, G.; Bugnazet, D.; Castillo-Michel, H.; Cornu, C.; Fayard, B.; Gagliardini, E.; Hino, R.; Morse, J.; Papillon, E.; Pouyet, E.; Rivard, C.; Solé, V.A.; Susini, J.; Veronesi, G. *J. Phys.: Conf. Ser.* **2013**, *425*, 182004.
- ³⁹ Ravel, B.; Newville, M. *J. Synchrotron Radiat.* **2005**, *12*, 537-541.
- ⁴⁰ Schroer, C.G.; Boye, P.; Feldkamp, J.M.; Patommel, J.; Samberg, D.; Schropp, A.; Schwab, A.; Stephan, S.; Falkenberg, G.; Wellenreuther, G.; Reimers, N. *Nucl. Instrum. Methods Phys. Res., Sect. A* **2010**, *616*, 93-97.
- ⁴¹ De Nolf, W.; Vanmeert, F.; Janssens, K. *J. Appl. Crystallogr.* **2014**, *47*, 1107-1117.

- ⁴² Pantelouris, A.; Modrow, H.; Pantelouris, M.; Hormes, J.; Reinen, D. *Chem. Phys.* **2004**, *300*, 13-22.
- ⁴³ Tromp, M.; Moulin, J.; Reid, G.; Evans, J. *AIP Conf. Proc.* **2007**, *882*, 699-701.
- ⁴⁴ Peterson, M.L.; Jr Brown, G.E.; Parks, G.A.; Stein, C.L. *Geochim. Cosmochim. Acta* **1997**, *61*, 3399-3412.
- ⁴⁵ Farges, F. *Phys. Chem. Miner.* **2009**, *36*, 463-481.
- ⁴⁶ Levina, A.; Codd, R.; Foran, G.J.; Hambley, T.W.; Maschmeyer, T.; Masters, A.F.; Lay, P.A. *Inorg. Chem.* **2004**, *43*, 1046-1055.
- ⁴⁷ Eeckhout, S.G.; Safonova, O.V.; Smolentsev, G.; Biasioli, M.; Safonov, V.A.; Vykhodtseva, L.N.; Sikora, M.; Glatzel, P. *J. Anal. At. Spectrom.* **2009**, *24*, 215-223.
- ⁴⁸ MacMillan, S.N.; Walroth, R. C.; Perry, D.M.; Morsing, T.J.; Lancaster, K.M. *Inorg. Chem.* **2015**, *54*, 205-214.
- ⁴⁹ Safonov, V.A.; Vykhodtseva, L.N.; Polukarov, Y.M.; Safonova, O.V.; Smolentsev, G.; Sikora, M.; Eeckhout, S.G.; Glatzel, P. *J. Phys. Chem. B* **2006**, *110*, 23192-23196.
- ⁵⁰ Torres Deluigi, M.; de Groot, F.M.F.; López-Díaz, G.; Tirao, G.; Stutz, G.; Riveros de la Vega, J. *J. Phys. Chem. C* **2014**, *118*, 22202-22210.
- ⁵¹ Gallo, E.; Glatzel, P. *Adv. Mater.* **2014**, *26*, 7730-7746.
- ⁵² Castillo-Michel, H.A.; Larue, C.; del Real, A.E.P.; Cotte, M.; Sarret, G. *Plant Physiol. Biochem.* **2017**, *110*, 13-32.
- ⁵³ Meents, A.; Gutmann, S.; Wagner, A.; Schulze-Briesse, C. *Proc. Natl. Acad. Sci. U.S.A.* **2010**, *107*, 1094-1099.
- ⁵⁴ Holton, J.M. *J. Synchrotron Radiat.* **2006**, *16*, 133-142.
- ⁵⁵ Weng, T.C.; van der Linden, P.J.; Glatzel, P.; Lapras, C.; Krzyzowski, M. *AIP Conf. Proc.* **2010**, *1234*, 617-620.
- ⁵⁶ Boesenberg, U.; Ryan, C.G.; Kirkham, R.; Siddons, D.P.; Alfeld, M.; Garrevoet, J.; Núñez, T.; Claussen, T.; Kracht, T.; Falkenberg, G. *J. Synchrotron Radiat.* **2016**, *23*, 1550-1560.

TOC



For Table of Contents Only